Hindawi
International Journal of Energy Research
Volume 2024, Article ID 5540018, 15 pages
https://doi.org/10.1155/2024/5540018

Research Article

Pd@CoFe Alloys on N-Doped Carbon Derived from Charred Tissue Paper as Synergistic Bifunctional Oxygen Electrocatalysts

Narayanamoorthy Bhuvanendran,[1] R. Selva Kumar,[2] and Sae Youn Lee[1]

[1]*Department of Energy and Materials Engineering, Dongguk University, Seoul 04620, Republic of Korea*
[2]*Department of Chemistry, Maharishi Markandeshwar Engineering College, Maharishi Markandeshwar (Deemed to be University), Mullana, Ambala, Haryana 133207, India*

Correspondence should be addressed to Sae Youn Lee; saeyounlee@dongguk.edu

Received 8 September 2023; Revised 4 February 2024; Accepted 16 February 2024; Published 14 March 2024

Academic Editor: Kisan Chhetri

Integrating more active components into a catalyst material could facilitate the development of multifunctional electrocatalysts for energy conversion and storage applications. In this study, we developed a multifunctional electrocatalyst, namely, Pd alloyed with Co-Fe deposited on N-doped mesoporous carbon derived from tissue paper (Pd@Co-Fe/N-TDC). The synergism in Pd@Co-Fe/N-TDC, stemming from the interatomic alloy between Pd and Co-Fe, N-doped mesoporous carbon with defective surfaces, distribution of polyhedral Pd nanoparticles, and strong metal-support interfacial interaction, resulted in significantly high electrocatalytic performance for both oxygen reduction reaction (ORR) and oxygen evolution reaction (OER). Pd@Co-Fe/N-TDC was found to be an efficient bifunctional oxygen electrocatalyst, and this was evidenced by a high onset potential (1.01 V) and kinetic current density (2.6 mA/cm^2) for the ORR and by a low overpotential (296 mV) and a low Tafel slope value (38 mV/dec) for the OER, along with a small ΔE of 736 mV. The catalyst also exhibited high durability for both ORR and OER, even after 10000 and 5000 cycles, respectively. Theoretical assessment provides an insight into the synergism of active metal sites in Pd@Co-Fe/N-TDC, which showed its potential for use as a non-Pt electrocatalyst for energy applications.

1. Introduction

The development of multifunctional electrocatalysts is a highly anticipated area of research aimed at tackling critical socioeconomic challenges in the energy and environmental sectors [1–3]. In the field of green energy technology, oxygen bifunctional electrocatalysts with multifunctional activity have tremendous potential to revolutionize sustainable energy conversion and storage systems [3–5]. These catalysts can play a pivotal role in the advancement of various electrochemical devices such as fuel cells, electrolyzers, and batteries by facilitating efficient energy conversion and the use of renewable energy sources [6, 7]. The kinetics of the oxygen reduction reaction (ORR) and oxygen evolution reaction (OER) depend on the electron transfer rate, surface adsorption of intermediates, and active sites accessibility, which are influenced by the structure-activity relationship of the catalyst during the electrochemical reactions [3, 8].

Generally, while noble-metal-based electrocatalysts are excellent for the ORR, they are less favorable for the OER, and vice versa, owing to the complex reaction mechanism [9, 10]. Hence, a well-engineered cost-effective multifunctional electrocatalyst with optimized performance is crucial for practical applications. In alkaline media, Pd-based electrocatalysts are good alternatives to Pt since their electronic and crystalline properties are comparable to those of Pt [11, 12]. Despite cost-effective measures, the modification of Pd's electronic structure is a critical strategy for achieving optimized electrocatalytic performance through increased accessibility of active sites, with strong electronic redistribution from adjacent secondary active elements [12–14]. Among nonnoble metals, Co has attracted considerable attention for its versatile electronic properties and efficient oxygen electrocatalysis when alloyed with Pd, owing to inherent oxygen defects in its oxide form [13–16]. Furthermore, bimetallic compounds, such as Co-Fe alloyed with

Pd, have been identified as promising electrocatalysts for the ORR, OER, and HER. In particular, the use of conventional carbon as a support for Pd-CoFe has a significant effect on the long-term electrocatalytic activity of the compound [17–21]. This finding has encouraged researchers to further investigate this combination through various strategic approaches, including enhancing the metal-support interaction for different carbon supports.

Multiple active components can be effectively integrated using a carbonaceous support, which enhances electron distribution and increases the surface reactivity of the active metal components because of its defective surface and highly accessible catalyst sites [1, 22, 23]. Furthermore, doping the carbon substrate with heteroatoms (such as N, S, and P) can significantly improve its electronic conductivity by delocalizing the π-electrons, resulting in noteworthy changes in the electronic and chemical activity of the catalysts [1, 3, 24–26]. In N-doped carbon, the closely matched atomic radii and significant electronegativity difference between N and C atoms allow facile heteroatom doping without altering the carbon skeleton. This facilitates electron redistribution and creates a favorable band potential for O_2 adsorption [27]. The active role of pyridinic and graphitic N-atoms within N-doped carbon structures in improving facile electron transfer to adjacent active metal sites has been underscored in the literature for the identification of active sites during oxygen electrocatalysis [28, 29]. Biomaterial-derived activated carbon with heteroatom doping has drawn significant attention because of its abundance, low cost, and sustainable recyclability, and it is a promising alternative to expensive and complex conventional carbon supports [30–32]. In the case of metal nanoparticles that adhere strongly to supporting materials, highly favorable electron transfer occurs between them, which is induced by a strong metal-support interfacial interaction [33–35]. Consequently, this phenomenon may enhance the synergistic effects of the catalysts through inherent electronic and geometric changes, leading to superior multifunctional electrocatalytic performance [36, 37].

Considering the aforementioned key aspects of engineering multifunctional electrocatalysts, we designed and developed polyhedral Pd nanoparticles alloyed with Co-Fe and decorated them on an N-doped carbon support (Pd@Co-Fe/N-TDC) derived from charred laboratory tissue papers. Pd@Co-Fe/N-TDC was synthesized using a two-stage method. First, Co-Fe with a bipyridine complex was grown on pretreated tissue paper, and it was then subjected to carbonization. Subsequently, Pd nanoparticles were decorated onto the substrate by using a chemical reduction method, and they were activated through pyrolysis. Furthermore, monometallic Co and Fe and bimetallic Co-Fe on N-TDC were studied and compared for oxygen electrocatalysis. Compared with the commercial standard Pt/C used for the ORR, Pd@Co-Fe/N-TDC exhibited a higher onset potential (1.01 V) and mass activity (2.6 mA/cm^2 at 0.85 V). Additionally, it showed a lower overpotential (296 mV) and a higher current density (0.702 mA/μg_{Pd}) during the OER compared with other catalysts, including the standard RuO_2. The catalyst had exceptional durability, and it could withstand 10,000 potential cycles during the ORR, with negligible half-wave potential shift and only a small increase in the overpotential for the OER after 5000 cycles. Pd@Co-Fe/N-TDC exhibited enhanced oxygen bifunctional performance that could be attributed to its high specific surface area, mesoporosity, surface defects, N-C conjugation, uniform distribution of Pd nanoparticles, strong interatomic alloy formation, and improved metal-support interfacial interaction, all of which synergistically contributed to its superior performance.

2. Experimental Section

2.1. Preparation of CoFe Alloy on N-Doped Carbon Derived from Tissue Paper (Co-Fe/N-TDC). First, 5 g of laboratory wipe tissue paper (TP) was pretreated by soaking it in an ethanol/water mixture for 6 h and then in an acetone/water mixture overnight. The treated solvents were completely drained, and the soaked TP was dried for 24 h at 90°C. Second, Co-Fe alloy crystals were grown by mixing 0.23 g of cobalt nitrate hexahydrate ($Co(NO_3)_3{\cdot}6H_2O$), 0.50 g of iron nitrate nonahydrate ($Fe(NO_3)_3{\cdot}9H_2O$), and 0.39 g of 2,2′-bipyridine (Bpy) in 25 ml of an ethanol/water mixture (1 : 1). The mixture was left to slowly evaporate, giving rise to the formation of a needle-shaped crystal complex, as depicted in Figure S1. The Co-Fe alloy crystals formed were then redispersed in ethanol and mixed with the pretreated TPs by soaking them overnight, and this was followed by drying for 24 h at 90°C. Finally, the dried Co-Fe alloy-coated TPs were calcinated for 6 h at 550°C and washed with 0.1 M HCl to remove any untreated residues. They were then washed with water until their pH was neutral. The final yield was further activated by pyrolysis treatment for 90 min at 850°C in an argon atmosphere. A similar synthesis method has previously been used to prepare monometallic catalyst materials, namely, Co/N-TDC and Fe/N-TDC, with the amounts of metal precursor used being 0.46 and 1.01 g, respectively. Here, the abbreviation TDC represents carbon derived from TP.

2.2. Synthesis of Low-Loading Pd on Co-Fe Alloy/N-Doped Carbon (Pd@Co-Fe/N-TDC). To achieve a low (10%) Pd loading on CoFe/N-TDC, we dispersed 100 mg of CoFe/N-TDC in 25 ml of ethylene glycol (EG) under vigorous stirring for 30 min. Then, 250 μl of 1 mM KBr in EG/H_2O and 4.89 mg of K_2PdCl_4 were taken in a three-necked round-bottom flask at room temperature and continuously stirred for 30 min. Finally, 5 ml of 0.05 M ascorbic acid was injected into the reaction mixture in an inert atmosphere (nitrogen gas) at a temperature of 110°C (achieved using an oil bath) under continuous stirring for 60 min. After the reaction was complete, the resulting mixture was cooled to room temperature, and the final product was collected through centrifugation. The collected product was then washed with a copious amount of water/ethanol mixture and dried at 90°C for 6 h.

2.3. Characterization Techniques. The crystallinity of the catalyst materials was investigated using powder X-ray diffraction (XRD) analysis conducted with an Ultima IV/Rigaku instrument. A Cu Kα source with a wavelength of 1.5409 Å was used for XRD measurements. The morphology of the

catalysts was analyzed using high-resolution transmission electron microscopy (HRTEM), performed with a JEM-2100 (JEOL, 200 kV) microscope. Elemental distribution and composition were determined using a combination of scanning transmission electron microscopy (STEM), high-angle annular dark field (HAADF) imaging, and energy dispersive X-ray spectroscopy (EDX) on an FEI Tecnai G2 F20 (200 kV) instrument. The porosity and specific surface area of the catalysts were determined using the Brunauer–Emmett–Teller (BET) analysis method and a Tristar II 3020 instrument. The surface properties of the catalyst materials were determined using Raman spectroscopy, with a DXR instrument from Thermo Fisher. The precise atomic weight percentages of noble and nonnoble elements in the catalyst materials were estimated using an inductively coupled plasma-mass spectrometer (ICP-MS) such as the Agilent 7000 instrument. The electronic properties of the catalyst materials were investigated through X-ray photoelectron spectroscopy (XPS) measurements performed on a Versa Probe II instrument (ULVAC-PHI), with Al Kα monochromatic rays as the excitation source.

2.4. Electrochemical Measurements. A three-electrode cell setup comprising a glassy carbon-rotating disc working electrode (GC-RDE, geometric area: 0.196 cm^2), a saturated calomel reference electrode (sat. KCl), and a graphite rod as the counter electrode on an electrochemical workstation (ZIVE SP1, South Korea) was used along with an RDE rotator (ALS, Japan). The RDE-GC was polished to mirror finish, and exactly 10 μl of a catalyst ink was drop casted followed by normal drying at ambient conditions. The catalyst ink was prepared by ultrasonicating 3.0 mg of the catalyst in a mixture of 1 ml absolute ethanol + 20 μl-diluted (5 wt%) Nafion for 10 min. For all electrochemical experiments, the final catalyst loading was maintained at 15 $\mu g/cm^2{}_{Pd}$ for Pd@Co-Fe/N-TDC, while the other nonnoble metal-based catalysts had a loading of approximately 150 $\mu g/cm^2$. Commercial Pt/C and RuO_2 catalysts were loaded at around 30 $\mu g/cm^2$ for all electrochemical experiments.

For the ORR measurements, cyclic voltammograms (CV) were recorded in N_2-saturated 0.1 M KOH electrolyte at a scan rate of 50 mV/s under ambient conditions. Linear scan voltammograms (LSV) were obtained in an O_2-saturated electrolyte at various rotation rates of the rotating disk electrode (RDE-GC), ranging from 400 to 2400 rpm, with a scan rate of 10 mV/s. The catalyst's stability during the ORR was assessed by subjecting it to continuous potential cycling (accelerated durability test, ADT) between 0.6 and 1.0 V at a scan rate of 100 mV/s. To evaluate the OER performance of the catalysts, we recorded LSV profiles in an N_2-saturated electrolyte at a scan rate of 10 mV/s while maintaining a rotation rate of 1600 rpm. The stability test for the OER was conducted under conditions identical to those employed for the ORR measurements. Furthermore, chronoamperometry (CA) analysis was performed at a potential of 1.53 V for a duration of 6000 s under N_2-saturated electrolyte conditions while maintaining a static electrode setup. All potentials are reported relative to the reversible hydrogen electrode (RHE).

2.5. Computational Methods. All density functional theory-(DFT-) based computational calculations were performed using the Gaussian 09 program package [38] with the aid of the GaussView visualization program. The ground state geometries were fully optimized using the hybrid B3LYP functional methods in combination with the 6-311G (d, p) basis set for lighter elements and LanL2DZ effective core potential for metals (Co, Fe, and Pd) [39]. All geometries were optimized to zero negative vibrational frequency to ensure the global minima. The fractional contributions of various fragments to each density of state (DOS) were plotted by using Multiwfn [40], and Chemissian was used for data interpretation. The electrostatic potential map and spin density was plotted using GaussView with isovalues of 0.02 and 0.002, respectively.

3. Results and Discussion

Figure 1(a) shows a pictorial representation of the sequential process used for fabricating the catalyst. It begins with the formation of the Co-Fe alloy on N-doped pretreated tissue paper. This is followed by carbonization and activation, which involve different heat-treatment approaches. Finally, polyhedral Pd nanoparticles are decorated onto the Co-Fe/N-TDC substrate through a mild cochemical reduction method. Figure 1(b) presents stacked XRD patterns of the catalysts, which were compared with the standard JCPDS files of potential elemental species. Notably, the Co-Fe/N-TDC sample showed sharp diffraction peaks at 44.8° and 65.0°, corresponding to the (110) and (200) planes of the CoFe alloy, respectively. These findings agreed well with JCPDS #049-1568 [41], distinguishing it from the XRD patterns of pristine Fe/N-TDC and Co/N-TDC.

Well-defined diffraction peaks corresponding to various crystallographic planes were observed in the Pd-decorated Co-Fe/N-TDC sample, as shown in the enlarged portion. These peaks corresponded to C(002), Pd(111), Pd(200), Pd(220), and CoFe(110) and occurred at diffraction angles of 24.4°, 40.3°, 46.7°, 68.4°, and 44.7°, respectively. The observed shift in the diffraction angle toward higher values for Pd planes (JCPDS #005-0681) [42] and toward lower values for Co-Fe alloy planes provides valuable insights into the atomic-level interactions between Pd and Co-Fe. An analysis of the XRD data facilitated the determination of key parameters for the Pd(111) plane, including the d-spacing value, lattice parameter, and percentage of lattice strain. The calculated values were 0.224 nm, 0.3871 Å, and 0.031%, respectively. These results provide robust evidence of the formation of a strong interatomic alloy of Pd and Co-Fe. Additionally, the average crystallite size was estimated to be 6.6 nm from the Debye–Scherrer equation, which provided insights into the size of the crystalline domains in the alloy [41].

The catalytic performance of an electrocatalyst is significantly influenced by the specific surface area and porosity of the substrate material, as they determine the accessibility of active sites. To assess the catalytic performance of Pd@Co-Fe/N-TDC, we performed the BET analysis. Figure 1(c) shows the N_2 adsorption/desorption profile, which shows a

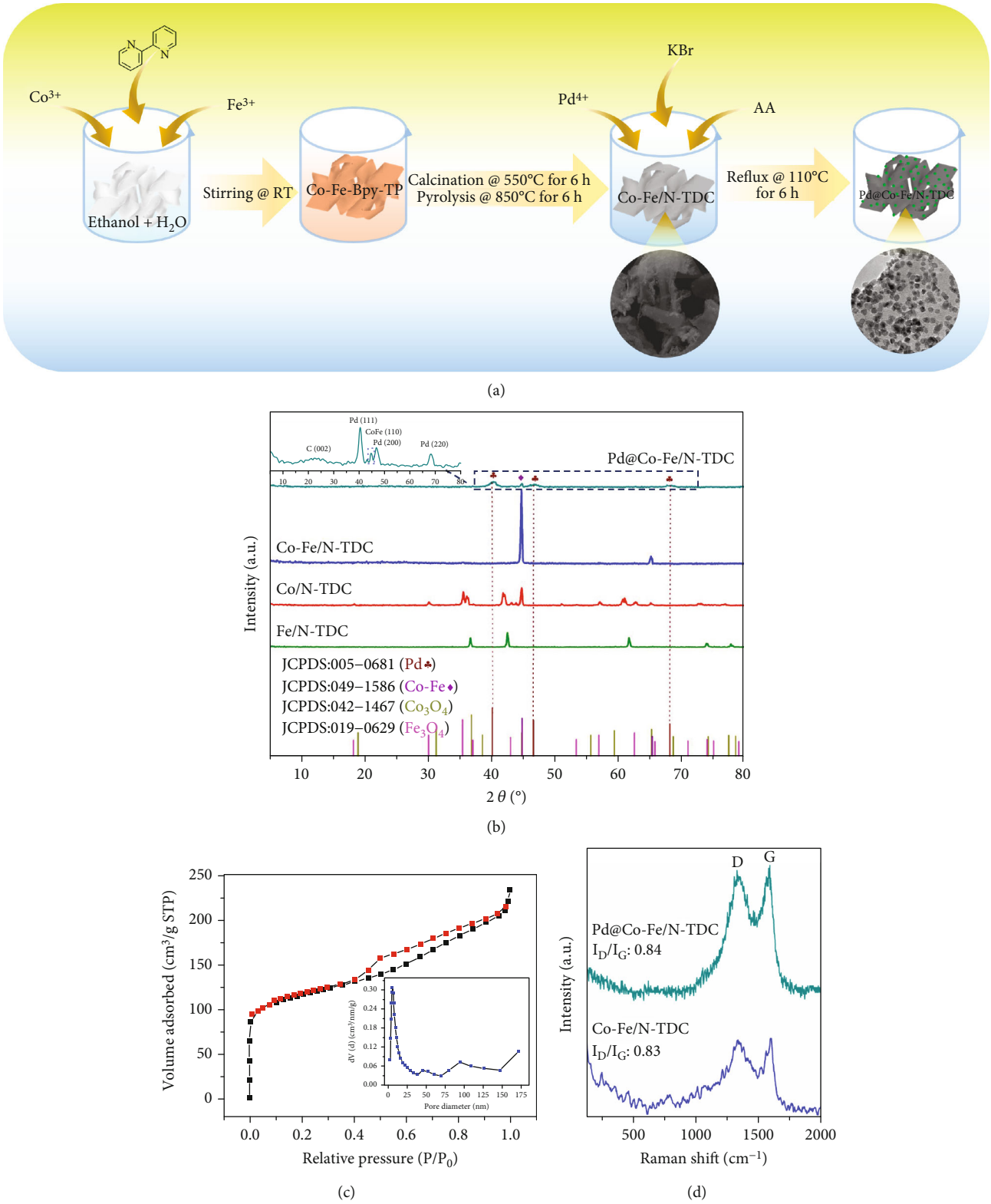

Figure 1: (a) Schematic representation of the preparation of the Pd@Co-Fe/N-TDC catalyst; (b) XRD patterns of Fe/N-TDC, Co/N-TDC, Co-Fe/N-TDC, and Pd@Co-Fe/N-TDC catalysts; (c) N_2-adsorption/desorption profile for Pd@Co-Fe/N-TDC (inset: corresponding Barrett–Joyner–Halenda plot); and (d) Raman spectroscopy profiles for the Co-Fe/N-TDC and Pd@Co-Fe/N-TDC catalysts.

characteristic type-IV isotherm with hysteresis loops, indicating the mesoporous nature of the catalyst. The specific surface area (SSA) was measured to be approximately 410.05 m^2/g, while the average pore diameter was determined to be 3.4 nm, as shown in the pore size distribution plot (inset of Figure 1(c)). In order to evaluate the degree

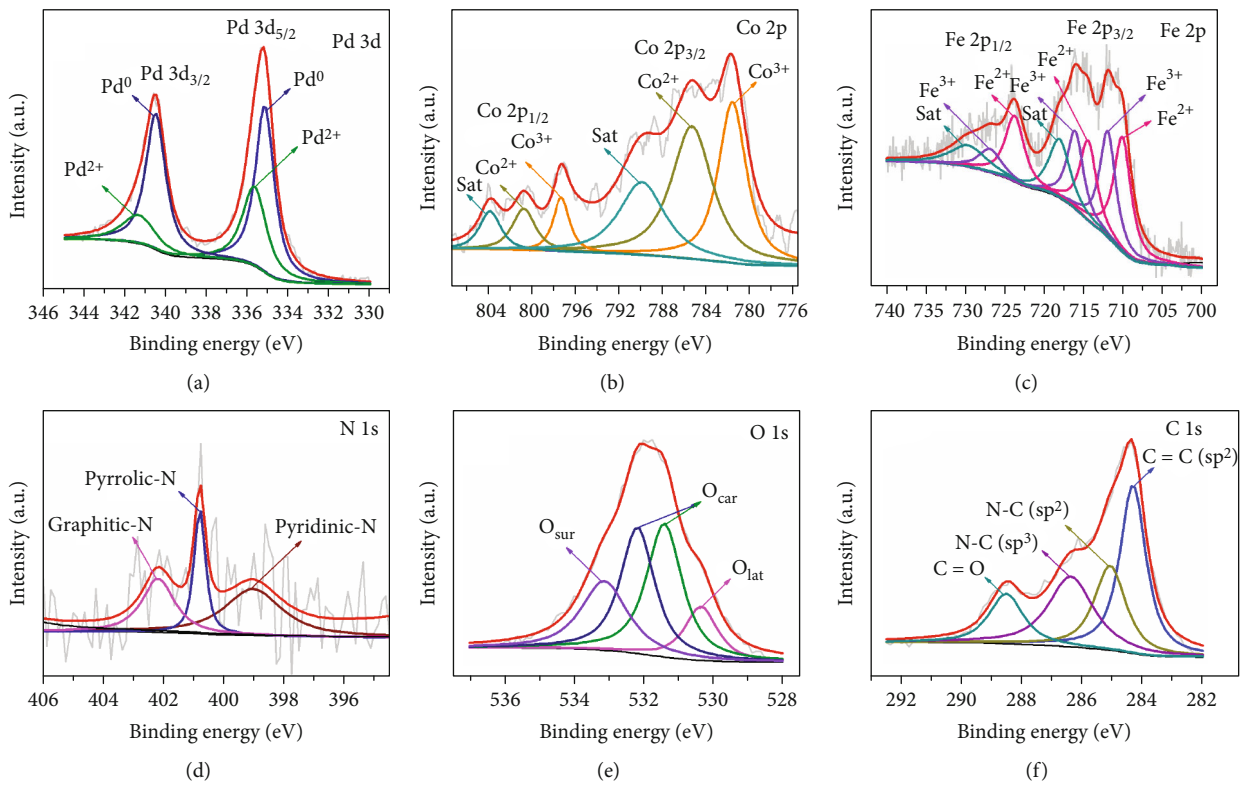

Figure 2: Deconvoluted XPS profiles of (a) Pt 3d, (b) Co 2p, (c) Fe 2p, (d) N 1s, (e) O 1s, and (f) C 1s for the Pd@Co-Fe/N-TDC catalyst.

of graphitization and surface defects in the carbon support of the Pd@Co-Fe/N-TDC and Co-Fe/N-TDC catalysts, we performed Raman spectra analysis; the results are presented in Figure 1(d). A set of well-defined characteristic peaks was observed at 1330.8 and 1583.1 cm^{-1}, corresponding to the disorder or defects (D-band) and crystalline nature (G-band) of the carbon support, respectively. The peak intensity of the D-band was found to be slightly lower than that of the G-band, which indicates the presence of sp^2-hybridized carbon in the catalyst substrate [21, 43]. Additionally, the I_D/I_G ratio for Pd@Co-Fe/N-TDC and Co-Fe/N-TDC is below 1, indicating greater structural order and a more graphitic nature on the catalysts' surface. This characteristic has the potential to enhance the kinetics of oxygen electrocatalysis [41, 44].

To ascertain the chemical state and atomic composition of the various elements (such as Pd, Co, Fe, C, N, and O) present in the catalyst, high-resolution XPS analysis was performed for Pd@Co-Fe/N-TDC. In Figure 2(a), the XPS spectrum of Pd 3d is presented, and it shows the deconvolution of doublets into $3d_{5/2}$ and $3d_{3/2}$ peaks. These doublets correspond to the metallic state (Pd^0) observed at 335.2 eV and 340.6 eV, and to the oxide state (Pd^{2+}) observed at 335.7 eV and 341.4 eV. The presence of distinct valence states of Pd, with a spin-orbit coupling constant of approximately 5.3 eV, is clearly evident [45]. In particular, the Pd^0/Pd^{2+} peak intensity ratio, which ranges from approximately 1.53 to 1.8, indicates the predominance of the metallic state of Pd in Pd@Co-Fe/N-TDC. The deconvoluted XPS peaks for both Co 2p and Fe 2p (Figures 3(b) and 3(c)) exhibit a doublet of doublets, indicating the presence of two distinct oxidation states: Co^{3+}/Co^{4+} and Fe^{2+}/Fe^{3+}. Additionally, the presence of adjacent shake-up satellite peaks suggests that both elements exist in a metal oxide form [16]. Interestingly, the binding energy of Pd^0 in Pd@Co-Fe/N-TDC was observed to be 0.4 eV lower than the standard Pd-metal value of 335.6 eV [46]. This negative shift in the binding energy indicates the possibility of interatomic interaction through electron coupling between Pd and the Co-Fe/N-TDC substrate. In Figure 2(d), the N 1s spectra show the presence of pyridinic-N, pyrrolic-N, and graphitic-N, which are distinct nitrogen species. Pyridinic-N and graphitic-N serve as recognized active sites, facilitating facile electron transfer with active metal sites in oxygen electrocatalysis, as documented in the literature [28, 29]. Furthermore, the XPS of O 1s (Figure 2(e)) and C 1s (Figure 2(f)) reveals strong elemental interactions among metal, carbon, and oxygen atoms, highlighting the presence of versatile active components in the catalyst.

The FE-SEM images in Figure S2a and S2b reveal a sheet-like morphology for the carbon derived from the tissue paper, with embedded metal nanoparticles, and TEM and HRTEM images (Figures 3(a) and 3(b)) showed a well-distributed arrangement of polyhedral Pd nanoparticles on the Co-Fe/N-TDC catalyst substrate. The Pd nanoparticles exhibited clear crystalline boundaries and were embedded within multiple layers of the Pd@Co-Fe/N-TDC catalyst. The average particle size distribution of the Pd nanoparticles was estimated to be 5.64 ± 0.9 nm from a histogram profile (inset of Figure 3(a)). Additionally, the interplanar distance (d-spacing) of the Pd(111) and Pd(200) planes was measured to be 0.224 nm and

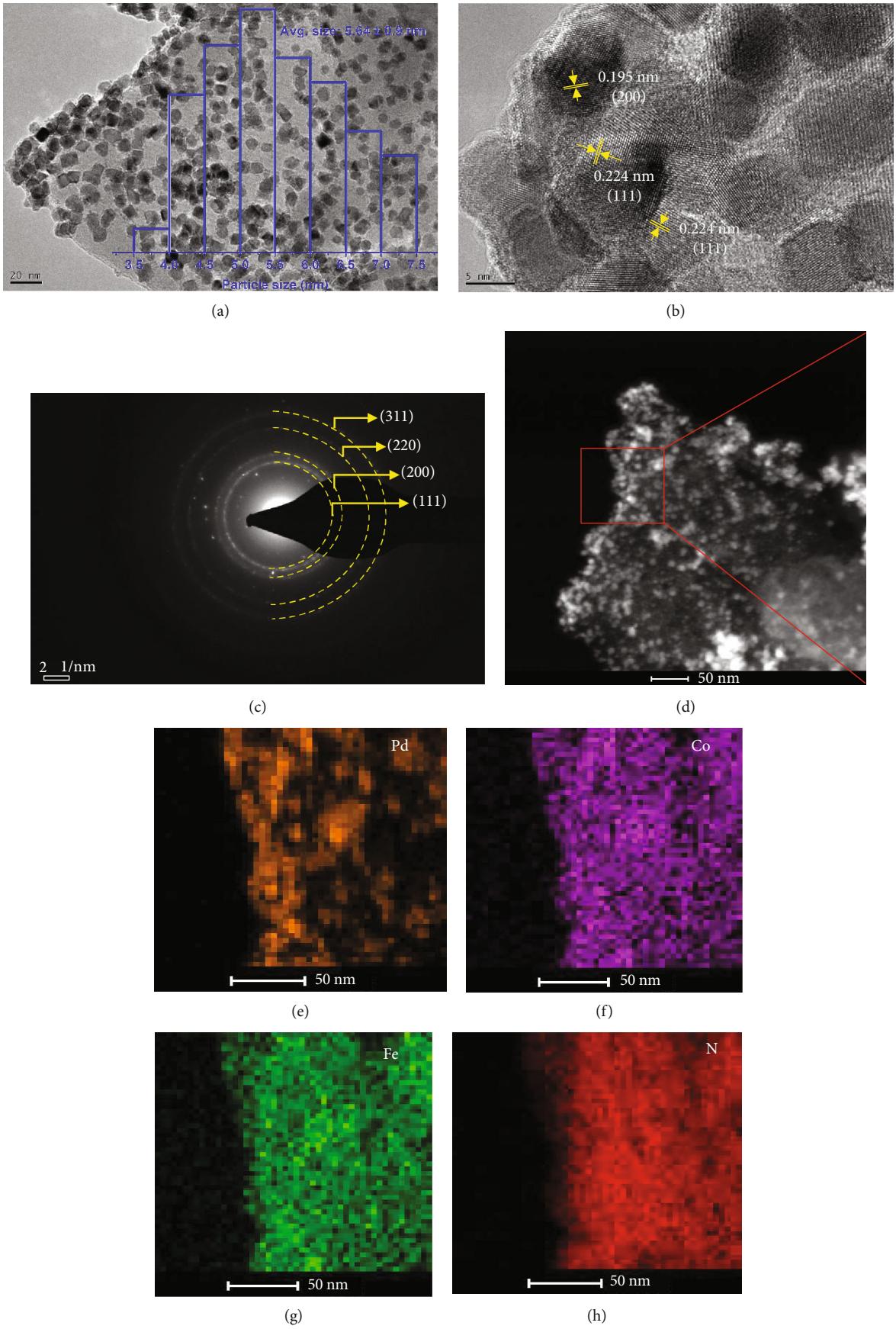

Figure 3: Continued.

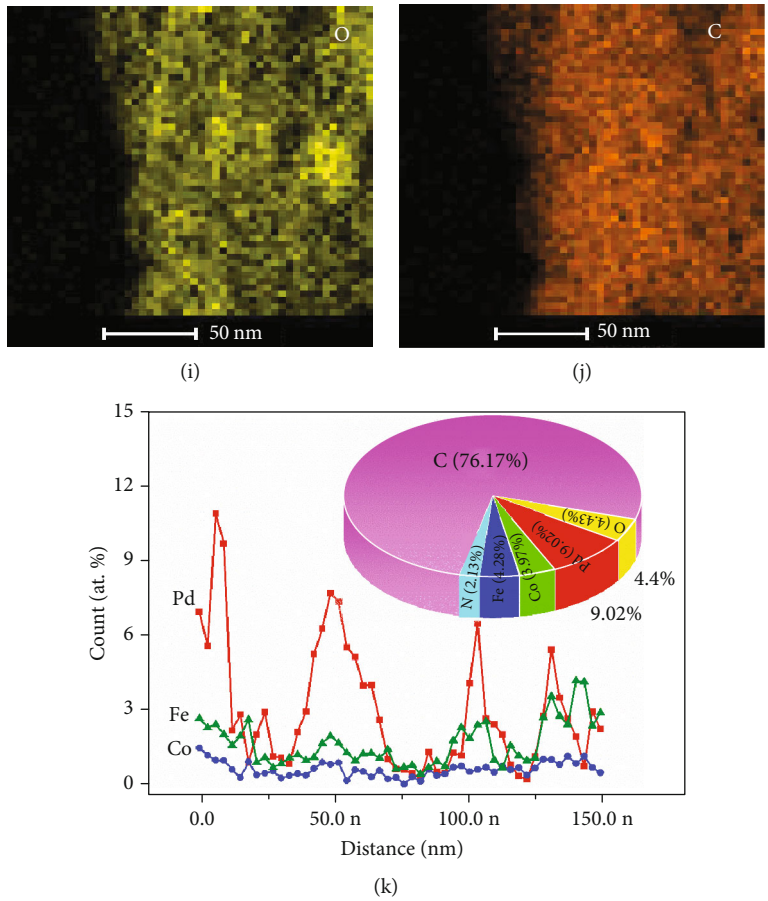

Figure 3: (a) TEM (inset: corresponding histogram profile) and (b) HRTEM images, (c) SAED pattern, (d) HAADF-STEM image with (e–j) corresponding elemental mappings, and (k) EDX-line scan profiles of Pd, Co, and Fe elements for the Pd@Co-Fe/N-TDC catalyst (inset: respective elemental distribution obtained from EDX).

0.195 nm, respectively, as indicated in Figure 3(b). In particular, the measured d-spacing value for Pd(111) was consistent with the XRD data, and it was noticeably smaller than that of the pristine Pd(111) plane (0.227 nm) [14]. This suggests the formation of a strong alloy of Pd and the other metals present in the catalyst. Figure 3(c) depicts SAED patterns with distinct diffraction rings corresponding to various crystalline planes, providing strong evidence for the existence of multiple crystalline domains in the Pd nanoparticles.

Figures 3(d)–3(j) show HAADF-STEM images along with the corresponding elemental mappings of Pd, Co, Fe, N, C, and O atoms. These elements were apparently uniformly distributed in the Pd@Co-Fe/N-TDC catalyst. The images in Figures 3(e)–3(g) show a significant overlap in the distributions of Pd, Co, and Fe atoms, indicating that strong interatomic interaction led to the formation of the alloy. Furthermore, the homogeneous distributions of N and C elements in the images (Figures 3(h) and 3(j)) indicate effective N-doping of the carbon support derived from tissue paper. EDX-line scan profiles of Pd, Co, and Fe metal atoms showed that the Pd@Co-Fe/N-TDC catalyst had a Pd-rich surface (Figure 3(k)). The higher concentration of Pd at the top layer enhanced the accessibility of active catalyst sites for oxygen electrocatalysis. The elemental composition of the Pd@Co-Fe/N-TDC catalyst was determined from its EDX profile (Figure S3), and the atomic weight percentage of each element is presented in the inset of Figure 3(k). Additionally, the percentage atomic composition of Pd, Co, and Fe was determined using ICP-MS analysis, and values of 9.8%, 45.6%, and 32.6% were obtained, respectively.

To assess the electrocatalytic behavior of the catalysts, we recorded their cyclic voltammogram profiles in N_2 and O_2-saturated 0.1 M KOH solutions under static conditions and compared the profiles (Figure S4). Under O_2-saturated conditions, all four electrocatalysts exhibited a distinct oxide-reduction peak during the cathodic sweep of the CVs. By contrast, there was no such peak in the N_2-saturated electrolyte, highlighting their capability for oxygen electrocatalysis. The Pd@Co-Fe/N-TDC catalyst outperformed other catalysts, with a higher oxide-reduction potential (0.71 V) and current density (1.12 mA/cm^2) than Co-Fe/N-TDC (0.46 V and 0.74 mA/cm^2), Co/N-TDC (0.46 V and 0.72 mA/cm^2), and Fe/N-TDC (0.57 V and 0.70 mA/cm^2). The higher values show the superior oxygen electrocatalysis in the case of Pd@Co-Fe/N-TDC compared with the other catalysts.

The ORR performance of all four catalysts, along with standard Pt/C, was studied by recording the polarization curves (LSV) in O_2-saturated 0.1 M KOH at 1600 rpm and a scan rate of 0.01 V/s; the curves are shown in Figure 4(a).

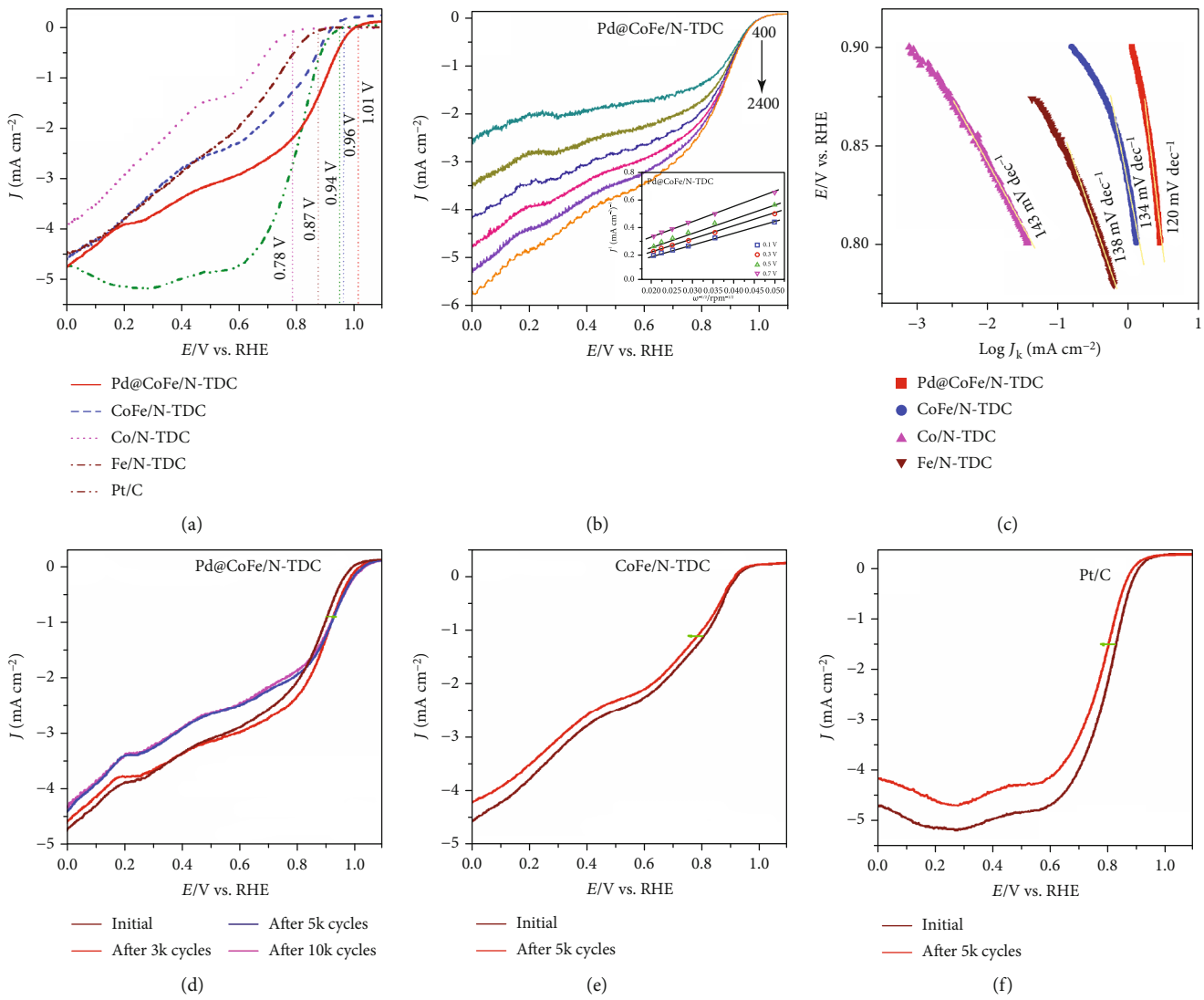

Figure 4: (a) LSV profiles recorded in O_2-saturated 0.1 M KOH at 1600 rpm and a scan rate of 0.01 V/s for all five catalysts, (b) LSV profiles at different rpm of the electrodes for Pd@Co-Fe/N-TDC (inset: respective K-L plot), (c) Tafel plots, and ADT-LSV profiles for the (d) Pd@Co-Fe/N-TDC, (e) Co-Fe/N-TDC, and (f) Pt/C catalysts.

Notably, the improved ORR activity of Pd@Co-Fe/N-TDC was evident from its onset potential (E_{onset}, 1.01 V) and half-wave potential ($E_{1/2}$, 0.79 V), which were higher than (by 70 mV) and comparable to the values for commercial Pt/C (0.94 V and 0.80 V), respectively. These values were also significantly higher than those of the Co-Fe/N-TDC (0.96 V and 0.66 V), Co/N-TDC (0.78 V and 0.42 V), and Fe/N-TDC (0.87 V and 0.54 V) catalysts, indicating the lower overpotential of Pd@Co-Fe/N-TDC that signified enhanced ORR kinetics. The kinetics of the ORR is related to the adsorption/dissociation of O_2 molecules at the catalyst site, with the metal-metal bond distance being the main factor determining the ORR performance [14, 47]. Notably, the formation of a strong interatomic alloy of Pd and adjacent metals (Co and Fe) in Pd@Co-Fe/N-TDC shifts the Pd d-band to the Fermi level, resulting in improved ORR kinetics, supported by kinetic parameters and XPS analysis.

The kinetic and diffusion-controlled ORR behavior of Pd@Co-Fe/N-TDC were evident in the LSVs recorded at different rotation rates (400–2400 rpm); the LSVs are depicted in Figure 4(b). The number of electrons transferred (n) during the ORR was determined from Koutecky–Levich (K-L) plots at different potentials (inset of Figure 4(b)). The linear and parallel K-L plots over the potential range for Pd@Co-Fe/N-TDC yielded an n value of 3.8, signifying the predominance of four-electron transfer during the ORR. Furthermore, the ORR kinetics of all four catalysts were evaluated by obtaining Tafel slope values from their respective Tafel plots, which are presented in Figure 4(c). The Tafel slope value of 120 mV/dec for Pd@Co-Fe/N-TDC was close to that of standard Pt/C and lower than the values of the other catalysts, indicating a higher rate of ORR kinetics on the catalyst. At 0.85 V, Pd@Co-Fe/N-TDC had a competitive kinetic current density (j_k, 2.6 mA/cm^2) and a competitive

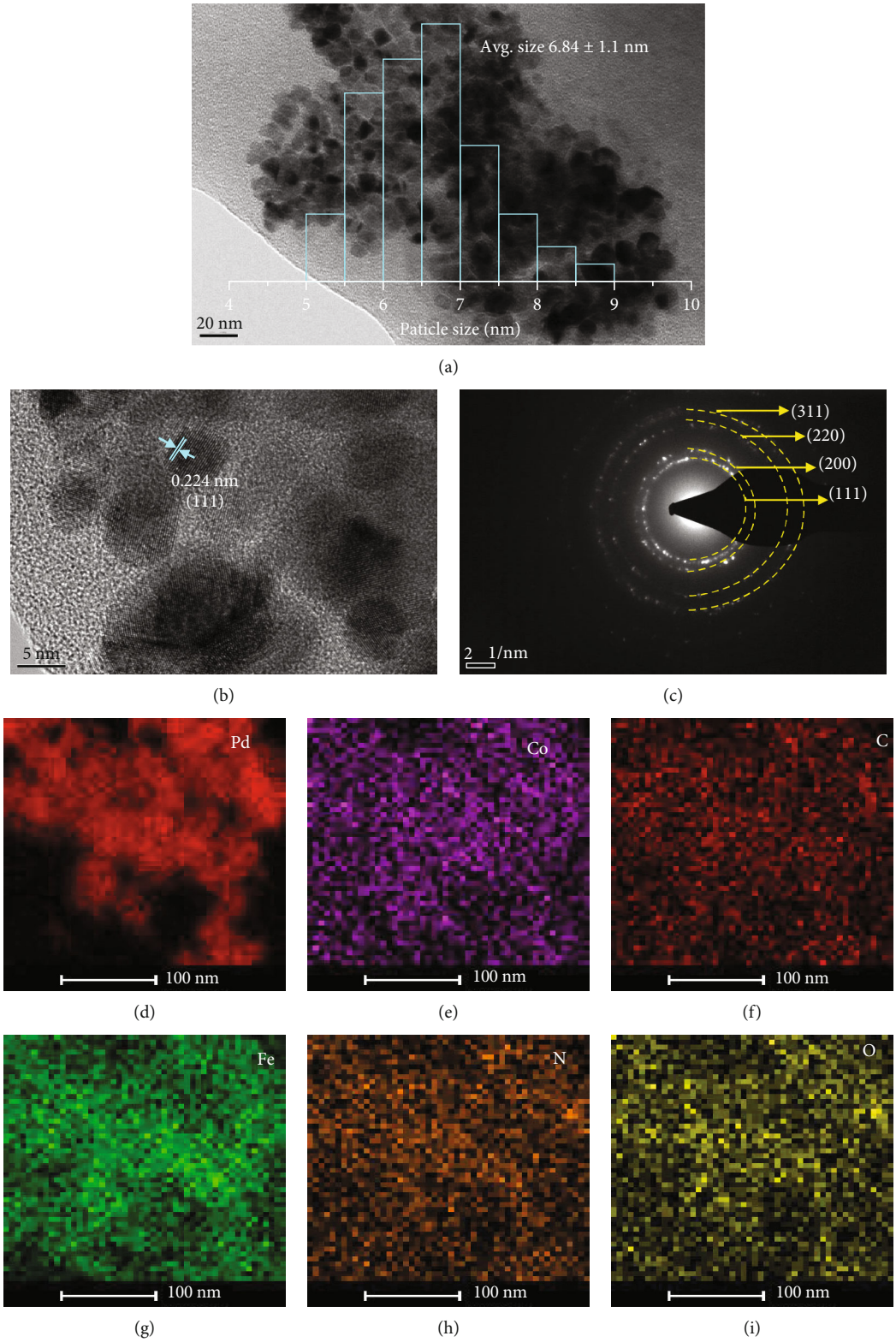

Figure 5: Continued.

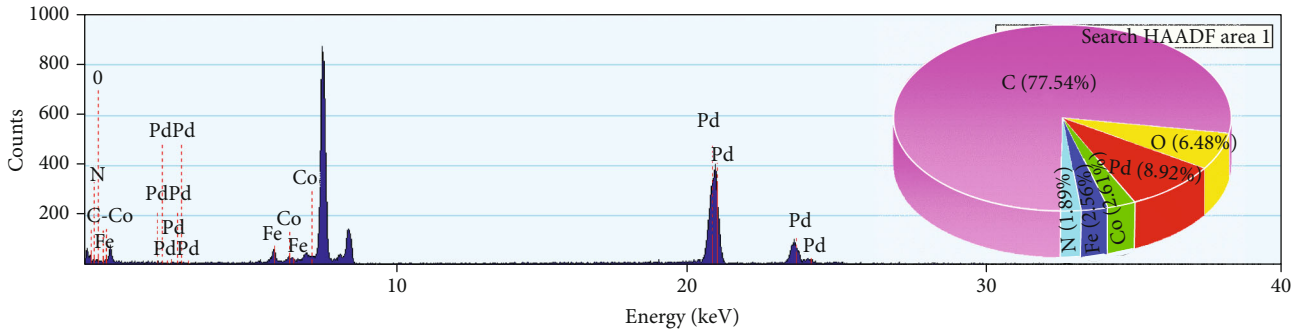

(j)

Figure 5: (a) TEM (inset: corresponding histogram profile) and (b) HRTEM images, (c) SAED pattern, (d–i) EDX elemental mappings, and (j) EDX profile for the Pd@Co-Fe/N-TDC catalyst (inset: respective elemental distribution) after the ORR durability test.

mass activity (MA, 0.173 mA/μg_{Pd}) compared with the other non-Pt catalysts reported for the ORR [17, 47].

The durability of Pd@Co-Fe/N-TDC during the ORR was examined by subjecting the catalyst to continuous potential cycling at 0.1 V/s under O_2-saturated conditions. Figure 4(d) shows the ORR-LSV, which was recorded to assess the key parameters at regular intervals of 3000, 5000, and 10000 cycles. After 3000 cycles, the E_{onset} and $E_{1/2}$ values shifted positively by around 10–20 mV, resulting in higher j_k (3.7 mA/cm^2) and MA (0.25 mA/μg_{Pd}) values at 0.85 V. These values were mostly retained after 5000 and 10000 cycles, with minimal changes, except for a significant difference in the diffusion limiting current between 0.8 and 0.1 V. The Co-Fe/N-TDC (Figure 4(e)) and Pt/C (Figure 4(f)) catalysts showed a negative shift of approximately 20–30 mV in E_{onset} and $E_{1/2}$ values after 5000 cycles, showing the high durability and sustained performance of Pd@Co-Fe/N-TDC during the ORR. A TEM image (Figure 5(a)) showed the morphological changes in the Pd@Co-Fe/N-TDC catalyst after 10000 cycles in the durability test. The microscopic images showed slight aggregation that led to particle size growth, and the average particle size was measured to be 6.84 nm, an increase of about 1 nm compared with its initial distribution. Figures 5(b) and 5(c) show the polycrystalline nature of Pd nanoparticles with dominant (111) planes. An interplanar distance of 0.224 nm was obtained from the HRTEM image, and various well-defined diffraction rings were observed in the SAED patterns. Furthermore, EDX mapping of the respective elements (Figures 5(d)–5(i)) clearly showed a nearly homogeneous distribution in the Pd@Co-Fe/N-TDC catalyst after durability studies. The atomic weight percentage of each element in Pd@Co-Fe/N-TDC showed a small decrease from the initial value obtained from the corresponding EDX profile (Figure 5(j)).

Apart from the ORR performance, we investigated the OER activities of all four catalysts by recording their LSV curves in N_2-saturated 0.1 M KOH at 1600 rpm and a potential scan rate of 10 mV/s and compared them with that of commercial RuO_2; the OER activities are shown in Figure 6(a). At an OER current density of 10 mA/cm^2, the Pd@Co-Fe/N-TDC catalyst exhibited an overpotential (η_{10}) of approximately 296 mV. This value is lower than those of the Co-Fe/N-TDC, Co/N-TDC, Fe/N-TDC, and RuO_2 catalysts by 7 mV, 82 mV, 136 mV, and 72 mV, respectively. Furthermore, the OER current density estimated at 1.53 V was found to be 0.702 mA/μg_{Pd}, which was nearly 10–15 times that of the other catalysts, including RuO_2 (Figure 6(b)). To gain insights into the OER kinetics, we determined the corresponding Tafel slope values for the catalysts. As shown in Figure 6(c), Pd@Co-Fe/N-TDC exhibited a lower slope value of 38 mV/dec compared with the other catalysts. These key parameters of OER indicate the fast kinetics on Pd@Co-Fe/N-TDC because of its superior electrocatalytic performance compared with that of the other catalysts.

The OER stability of the catalysts was studied by performing continuous potential sweeping up to 5000 cycles at a scan rate of 0.1 V/s, and also through chronoamperometry studies at 1.6 V. Figures 6(d) and 6(e) show the LSV-OER curves for the Pd@Co-Fe/N-TDC and Co-Fe/N-TDC catalysts. These catalysts exhibited negative shifts of nearly 43 and 77 mV in the overpotential, respectively, after 5000 cycles. In particular, Pd@Co-Fe/N-TDC retained nearly 70% of its initial OER current density measured at 1.53 V, which was approximately 10–15 times higher than that of the Co-Fe/N-TDC catalyst (inset of Figure 6(f)). From the CA studies, it was observed that Pd@Co-Fe/N-TDC showed better attenuation up to 6000 s compared with the other catalysts (Figure 6(f)). These results collectively imply that Pd@Co-Fe/N-TDC exhibits high durability for the OER and competes with the reported Pd-based catalysts [15, 48]. To probe the morphological changes of the Pd@Co-Fe/N-TDC catalyst, TEM and HRTEM images were obtained after the OER durability test and illustrated in Figure S5. The TEM image clearly reveals distinct morphological changes, including considerable agglomeration, after the OER durability test. This observed transformation might contribute to the deviation in the electrocatalytic performance of Pd@Co-Fe/N-TDC over the test period. Furthermore, the HRTEM image indicates that the d-spacing value aligns well with the Pd(111) plane and remains quite similar to the initial observation [49–51]. The oxygen bifunctional activity of the catalysts was determined by calculating the potential difference (ΔE) between $E_{1/2}$ during the ORR and η_{10} during the OER

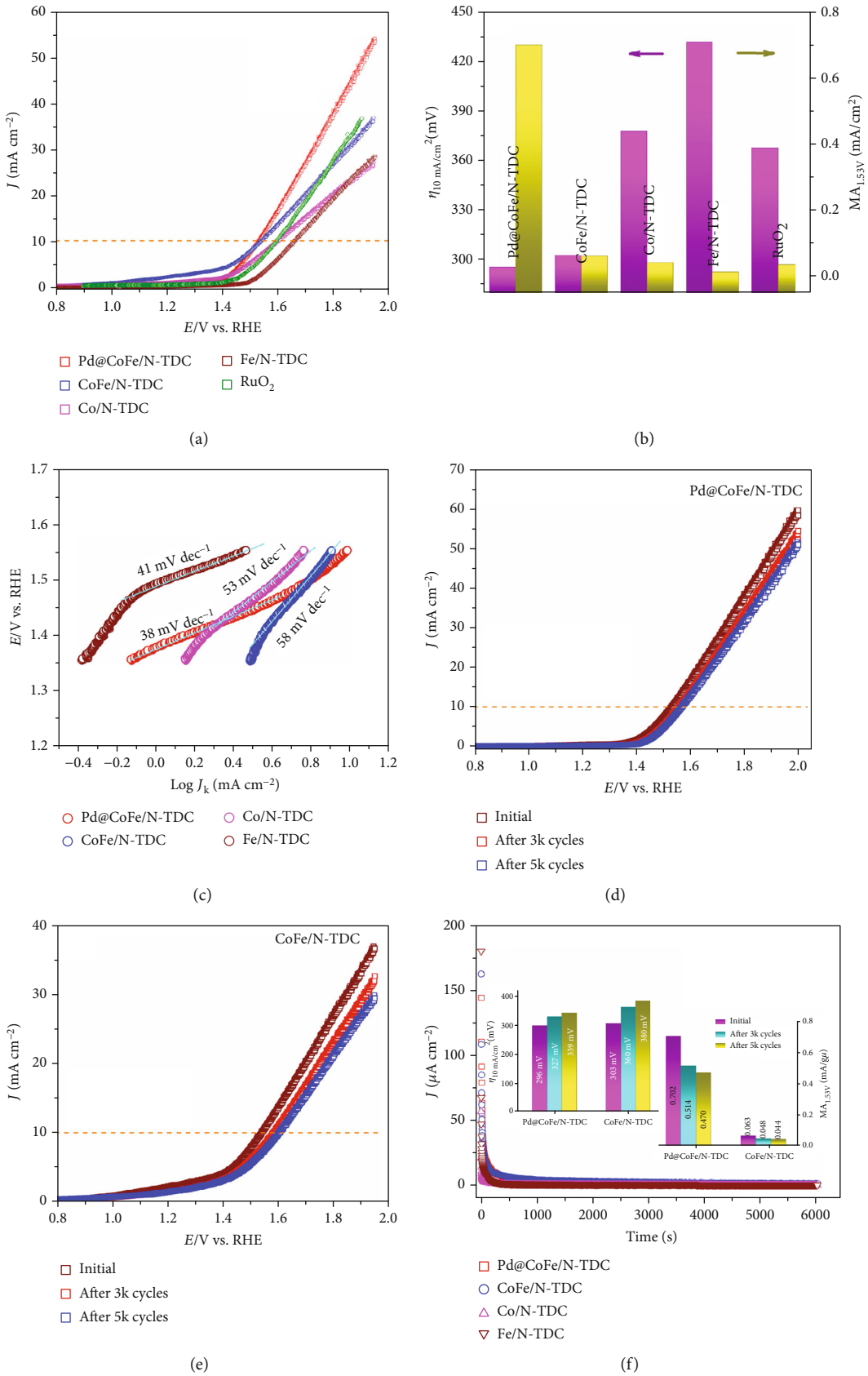

Figure 6: (a) LSV profiles recorded in N_2-saturated 0.1 M KOH at 1600 rpm and a scan rate of 0.01 V/s, (b) bar charts of the overpotential and OER mass activity for all five catalysts, (c) Tafel plots, and ADT-LSV profiles for (d) Pd@Co-Fe/N-TDC, (e) Co-Fe/N-TDC, and (f) chronoamperometry profiles at 1.53 V (inset: bar charts of changes in the overpotential and MA after a certain number of durability cycles).

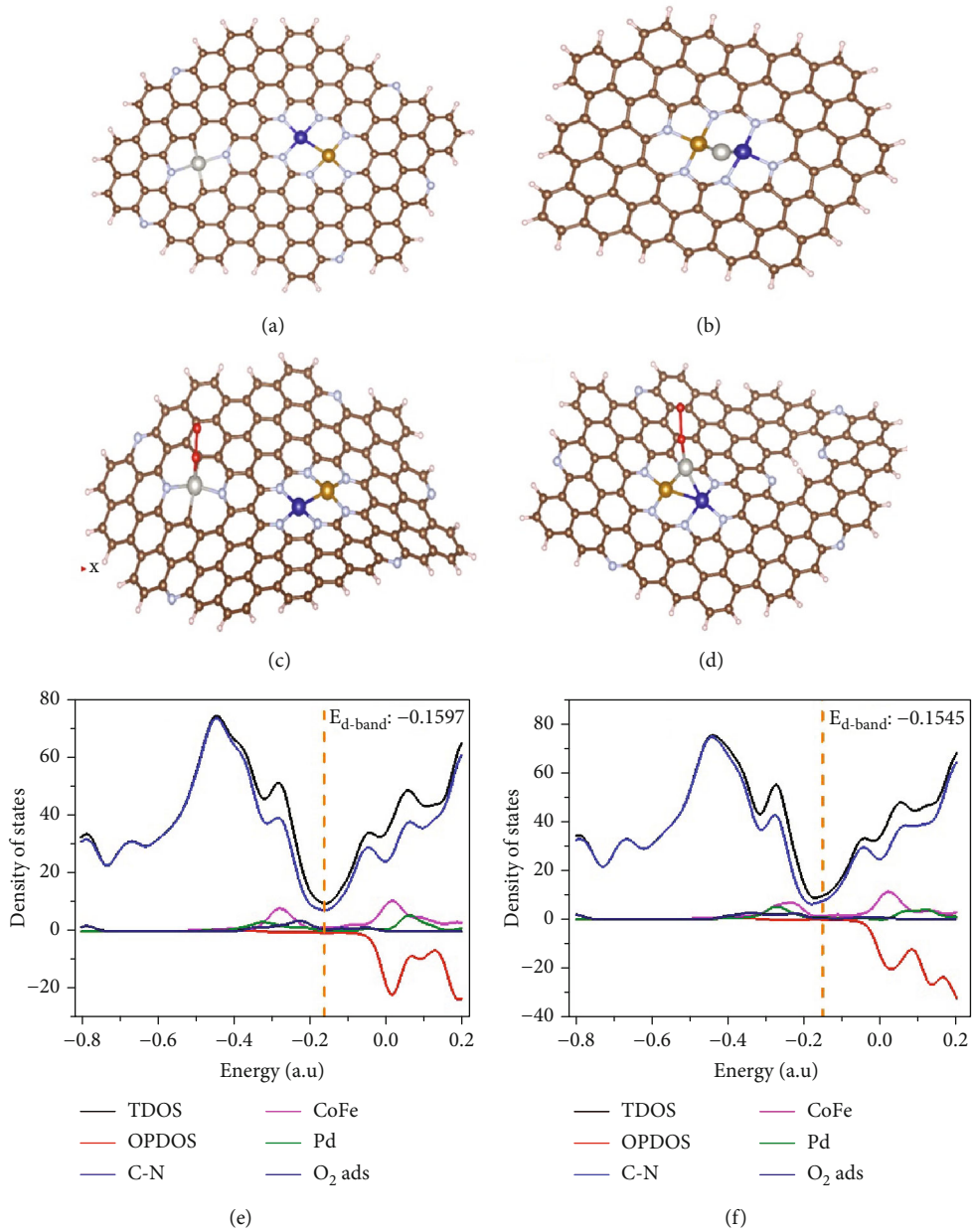

Figure 7: Top view of (a, b) initial and (c, d) the oxygen molecule adsorbed on different Pd@Co-Fe/N-TDC catalyst structures (STR1 and STR2) and (e, f) partial density of state profiles for different Pd@Co-Fe/N-TDC catalyst structures (STR1 and STR2 with the adsorption oxygen molecule.

[52, 53]. For Pd@Co-Fe/N-TDC, this potential difference was found to be 736 mV, which is comparatively lower than that of Co-Fe/N-TDC (836 mV) and other Pd-based electrocatalysts reported in the literature [13, 47, 54]. The lowest ΔE value indicated that Pd@Co-Fe/N-TDC had improved oxygen bifunctional activity with extended durability.

To assess catalyst synergies, DFT calculations were conducted to explore the energetically stable structural formations and synergistic effects among the active components. Two energy-optimized structures of the Pd@Co-Fe/N-TDC catalyst were proposed, showcasing notable distinctions in the distribution and interaction of active metal components. The top view of the catalyst sites in both structures, as depicted in Figures 7(a) and 7(b), reveals a consistent atomic-level interaction between Co and Fe, along with adjacent N-atoms. However, the Pd atom occupies different sites; in the first structure (Figure 7(a), STR1), it is bound with the C-N sites, while in the second structure (Figure 7(b), STR2), it directly interacts with the Co-Fe metallic sites. The electrostatic potential (ESP) mapping for both structures is displayed in Figures S6a and S6b, illustrating the atomic distribution of all elements including Pd, Co, and Fe metals. Notably, the ESP mapping reveals significant charge accumulation around the Pd metal site, especially in STR2. This heightened

charge density suggests a stronger interatomic interaction among Pd, Co, and Fe atoms compared to STR1, where Pd was isolated.

Furthermore, spin density plots for both STR1 and STR2 are depicted in Figures S6c and S6d, with blue representing positive and green indicating negative spin population. Notably, STR2 displays a significantly higher positive spin population compared to STR1, aligning well with the ESP mappings. This observation suggests a synergistic interaction among the three active metals Pd, Co, and Fe, intensifying surface reactivity with electronegative oxygen atoms (from O_2 or H_2O) during both ORR and OER [55]. Following oxygen molecule adsorption on Pd@Co-Fe/N-TDC catalyst structures (STR1 and STR2) in Figures 7(c) and 7(d), Pd—O bond length is 2.2469 Å, and the surface-adsorbed oxygen molecule (O—O) is 2.0200 Å in STR2, larger than in STR1. Therefore, the extended O—O bond length can facilitate efficient bond breaking, advancing to subsequent electrochemical reaction steps in ORR [56].

Additionally, the elongated metal-oxygen bond length may enhance the accessibility of active sites for further reactions on STR2 compared to STR1. Furthermore, the adsorption energy values indicate the interaction of surface oxygen molecules on active Pd sites in both STR1 and STR2. Additionally, the d-band shift was observed to be downshifted to the Fermi level for STR2 compared to STR1 (Table S1), which correlates well with the physicochemical results, particularly from XPS analysis. Theoretical calculations were conducted to illustrate the potential structural integration of trimetallic alloy formation in Pd@Co-Fe/N-TDC catalyst. These calculations emphasize the essential role of metal-metal interactions among Pd, Co, and Fe, enhancing surface reactivity for both ORR and OER and corroborating the synergistic effects of the catalysts.

The efficient electrocatalytic oxygen bifunctional activity and high durability of Pd@Co-Fe/N-TDC might be supported by the following crucial factors: (1) the uniform distribution of polyhedral Pd nanoparticles with distinct crystalline boundaries leads to a large number of structural interfaces and internal electron redistribution, enhancing the catalytic performance for the ORR and OER, (2) strong interatomic interaction between Pd and Co-Fe shifts the d-band center of Pd toward the Fermi level, reducing -OH adsorption at active sites and increasing the number of reactive sites for improved oxygen electrocatalysis, (3) the N-doped mesoporous TDC with high SSA improves the accessibility of active sites during surface reactions, (4) the strong metal-support interaction is a key factor influencing the electronic conductivity and structural integrity of the catalyst during electrochemical reactions, and (5) the polycrystalline properties of the Pd@Co-Fe alloy nanoparticles and the surface defects of the N-doped carbon substrate collectively contribute to the synergistic enhancement of the catalytic performance, rendering the catalyst an efficient bifunctional oxygen electrocatalyst.

4. Conclusion

A two-stage preparation process was successfully employed to synthesize a homogenous distribution of polyhedral Pd nanoparticles that could be alloyed with Co-Fe, embedded on a defect-rich and mesoporous N-doped carbon support derived from tissue papers. Heteroatom doping of TDC substantiates the electronic conductivity of the carbon support, facilitating strong interfacial interaction with the metal nanoparticles on it. This further synergized the electrocatalytic ability of Pd@Co-Fe/N-TDC by altering the Pd electronic structure through a downshift of the d-band center, thereby boosting the catalyst's performance for bifunctional oxygen electrocatalysis. With a high SSA and a defect-rich surface, the catalyst showed superior ORR performance (E_{onset}: 1.01 V; $E_{1/2}$: 0.79 V) compared with standard Pt/C. Furthermore, good OER activity (0.702 mA/μg_{Pd}) with a low η_{10} (approximately 296 mV) indicated better performance compared with standard RuO_2. The durability of Pd@Co-Fe/N-TDC was studied by ADT, and it showed a positive shift in $E_{1/2}$ with increased ORR activity, and approximately 70% retention of its OER activity with a ~43 mV negative shift in η_{10}. The overall performance of Pd@Co-Fe/N-TDC as an efficient oxygen bifunctional electrocatalyst was estimated with a low ΔE of 736 mV, and it was significantly higher than previously reported Pd-based catalysts. These findings point to the excellent electrocatalytic performance of Pd@Co-Fe/N-TDC over a long lifetime, highlighting its potential as a multifunctional non-Pt electrocatalyst for energy conversion and storage applications.

Data Availability

Data is available on request.

Conflicts of Interest

The authors declare that they have no known competing financial interests or personal relationships that could have appeared to influence the work reported in this paper.

Acknowledgments

This work was supported by a National Research Foundation (NRF) of Korea grant funded by the Korean government (MSIT) (No. RS-2022-00166466).

Supplementary Materials

Figure S1: optical image of Co-Fe/bipyridine crystal formation through slow-evaporation method. Figure S2: (a, b) FESEM images of Pd@Co-Fe/N-TDC catalyst. Figure S3: EDX profile of Pd@Co-Fe/N-TDC catalyst (inset: HAADF-STEM image). Figure S4: comparison of cyclic voltammograms recorded in N_2- and O_2-saturated 0.1 M KOH at a scan rate of 0.1 V/s for Fe/N-TDC, Co/N-TDC, Co-Fe/N-TDC, and Pd@Co-Fe/N-TDC catalysts. Figure S5: TEM and (b) HRTEM images of Pd@Co-Fe/N-TDC catalyst after the OER durability test. Figure S6: (a, b) electrostatic potential mappings and (c, d) spin density plots for different Pd@Co-Fe/N-TDC catalyst structures (STR1 and STR2). Table S1: key parameters from theoretical calculations for different Pd@Co-Fe/N-TDC catalyst structures (STR1 and STR2). *(Supplementary Materials)*

References

[1] Y. Zhang, M. Luo, Y. Yang, Y. Li, and S. Guo, "Advanced multifunctional electrocatalysts for energy conversion," *ACS Energy Letters*, vol. 4, no. 7, pp. 1672–1680, 2019.

[2] C.-X. Zhao, J.-N. Liu, J. Wang, D. Ren, B.-Q. Li, and Q. Zhang, "Recent advances of noble-metal-free bifunctional oxygen reduction and evolution electrocatalysts," *Chemical Society Reviews*, vol. 50, no. 13, pp. 7745–7778, 2021.

[3] S. Ghosh and R. N. Basu, "Multifunctional nanostructured electrocatalysts for energy conversion and storage: current status and perspectives," *Nanoscale*, vol. 10, no. 24, pp. 11241–11280, 2018.

[4] I. Katsounaros, S. Cherevko, A. R. Zeradjanin, and K. J. J. Mayrhofer, "Oxygen electrochemistry as a cornerstone for sustainable energy conversion," *Angewandte Chemie, International Edition*, vol. 53, no. 1, pp. 102–121, 2014.

[5] J. Zhang, Z. Zhao, Z. Xia, and L. Dai, "A metal-free bifunctional electrocatalyst for oxygen reduction and oxygen evolution reactions," *Nature Nanotechnology*, vol. 10, no. 5, pp. 444–452, 2015.

[6] B. Mohanty, P. Bhanja, and B. K. Jena, "An overview on advances in design and development of materials for electrochemical generation of hydrogen and oxygen," *Materials Today Energy*, vol. 23, article 100902, 2022.

[7] L. Peng and Z. Wei, "Catalyst engineering for electrochemical energy conversion from water to water: water electrolysis and the hydrogen fuel cell," *Engineering*, vol. 6, no. 6, pp. 653–679, 2020.

[8] S. Hou, R. M. Kluge, R. W. Haid et al., "A review on experimental identification of active sites in model bifunctional electrocatalytic systems for oxygen reduction and evolution reactions," *ChemElectroChem*, vol. 8, no. 18, pp. 3433–3456, 2021.

[9] H.-C. Li, Y.-J. Zhang, X. Hu, W.-J. Liu, J.-J. Chen, and H.-Q. Yu, "Metal–organic framework templated Pd@PdO–Co3O4 nanocubes as an efficient bifunctional oxygen electrocatalyst," *Advanced Energy Materials*, vol. 8, no. 11, article 1702734, 2018.

[10] G.-R. Zhang and S. Wöllner, "Hollowed structured PtNi bifunctional electrocatalyst with record low total overpotential for oxygen reduction and oxygen evolution reactions," *Applied Catalysis B: Environmental*, vol. 222, pp. 26–34, 2018.

[11] A. B. Yousaf, M. Imran, N. Uwitonze et al., "Enhanced electrocatalytic performance of Pt3Pd1 alloys supported on CeO2/C for methanol oxidation and oxygen reduction reactions," *The Journal of Physical Chemistry C*, vol. 121, no. 4, pp. 2069–2079, 2017.

[12] S. B. Kang, J. B. Lim, D. Jo et al., "Ostwald-ripening sintering kinetics of Pd-based three-way catalyst: importance of initial particle size of Pd," *Chemical Engineering Journal*, vol. 316, pp. 631–644, 2017.

[13] T. Hu, Y. Wang, L. Zhang et al., "Facile synthesis of PdO-doped Co3O4 nanoparticles as an efficient bifunctional oxygen electrocatalyst," *Applied Catalysis B: Environmental*, vol. 243, pp. 175–182, 2019.

[14] G.-R. Xu, C.-C. Han, Y.-Y. Zhu, J.-H. Zeng, J.-X. Jiang, and Y. Chen, "PdCo alloy nanonetworks–polyallylamine inorganic–organic nanohybrids toward the oxygen reduction reaction," *Advanced Materials Interfaces*, vol. 5, no. 4, article 1701322, 2018.

[15] Z. K. Ghouri, K. Elsaid, M. M. Nasef, S. Ahmed, A. Badreldin, and A. Abdel-Wahab, "Cooperative electrocatalytic effect of Pd and Ce alloys nanoparticles in PdCe@CNWs electrode for oxygen evolution reaction (OER)," *Molecular Catalysis*, vol. 522, article 112255, 2022.

[16] T. Yang, D. Bhalothia, H.-W. Chang et al., "Oxygen vacancies endow atomic cobalt-palladium oxide clusters with outstanding oxygen reduction reaction activity," *Chemical Engineering Journal*, vol. 454, article 140289, 2023.

[17] R. Manjunatha, L. Dong, Z. Zhai et al., "Pd nanocluster-decorated CoFe composite supported on nitrogen carbon nanotubes as a high-performance trifunctional electrocatalyst," *Green Energy & Environment*, vol. 7, no. 5, pp. 933–947, 2022.

[18] Z. Cui and X. Bai, "Highly active and stable Fe/Co/N Co-doped carbon-anchored Pd nanoparticles for oxygen reduction reaction," *ACS Applied Materials & Interfaces*, vol. 14, no. 7, pp. 9024–9035, 2022.

[19] A. Samanta and C. R. Raj, "Catalyst support in oxygen electrocatalysis: a case study with CoFe alloy electrocatalyst," *The Journal of Physical Chemistry C*, vol. 122, no. 28, pp. 15843–15852, 2018.

[20] B. Wang, K. Srinivas, Y. Liu et al., "N-doped CNTs capped with carbon layer armored CoFe alloy as highly stable bifunctional catalyst for oxygen electrocatalysis," *Nano Research*, vol. 15, no. 5, pp. 3971–3979, 2022.

[21] G. A. Gebreslase, D. Sebastián, M. V. Martínez-Huerta et al., "CoFe-loaded P, N co-doped carbon foam derived from petroleum pitch waste: an efficient electrocatalyst for oxygen evolution reaction," *Catalysis Today*, vol. 423, article 113991, 2023.

[22] X. Liu and L. Dai, "Carbon-based metal-free catalysts," *Nature Reviews Materials*, vol. 1, no. 11, article 16064, 2016.

[23] S. Das, A. Kundu, T. Kuila, and N. C. Murmu, "Recent advancements on designing transition metal-based carbon-supported single atom catalysts for oxygen electrocatalysis: miles to go for sustainable Zn-air batteries," *Energy Storage Materials*, vol. 61, article 102890, 2023.

[24] K. Gong, F. Du, Z. Xia, M. Durstock, and L. Dai, "Nitrogen-doped carbon nanotube arrays with high electrocatalytic activity for oxygen reduction," *Science*, vol. 323, no. 5915, pp. 760–764, 2009.

[25] Y. Zheng, Y. Jiao, Y. Zhu et al., "Hydrogen evolution by a metal-free electrocatalyst," *Nature Communications*, vol. 5, no. 1, p. 3783, 2014.

[26] A. Kundu, S. Bolar, S. Das et al., "General approach to synthesize multilayer graphitic carbon-nanotube-encapsulated NiCo alloys as trifunctional electrocatalysts: deciphering the role of N-dopants," *ACS Applied Energy Materials*, vol. 5, no. 11, pp. 14445–14454, 2022.

[27] H.-J. Zhang, Z. Zhou, Y. He, B. Chen, W. Yao, and Y. Xue, "How does metal affect N-doped carbon catalyst for oxygen reduction reaction?," *Journal of Electroanalytical Chemistry*, vol. 935, p. 117341, 2023.

[28] J. Quílez-Bermejo, M. Melle-Franco, E. San-Fabián, E. Morallón, and D. Cazorla-Amorós, "Towards understanding the active sites for the ORR in N-doped carbon materials through fine-tuning of nitrogen functionalities: an experimental and computational approach," *Journal of Materials Chemistry A*, vol. 7, no. 42, pp. 24239–24250, 2019.

[29] F. Kong, X. Cui, Y. Huang et al., "N-doped carbon electrocatalyst: marked ORR activity in acidic media without the

contribution from metal sites?," *Angewandte Chemie International Edition*, vol. 61, no. 15, article e202116290, 2022.

[30] X. Liu, C. Culhane, W. Li, and S. Zou, "Spinach-derived porous carbon nanosheets as high-performance catalysts for oxygen reduction reaction," *ACS Omega*, vol. 5, no. 38, pp. 24367–24378, 2020.

[31] N. Bhuvanendran, S. Ravichandran, M. Narayanan et al., "Emerging trends in biomass-derived carbon-supported metal nanostructures as efficient electrocatalysts for critical electrochemical reactions in low temperature fuel cell applications," in *Biorenewable Nanocomposite Materials, Vol. 1: Electrocatalysts and Energy Storage*, pp. 225–256, American Chemical Society, 2022.

[32] N. Bhuvanendran, S. Ravichandran, S. Kandasamy et al., "Spindle-shaped CeO2/biochar carbon with oxygen-vacancy as an effective and highly durable electrocatalyst for oxygen reduction reaction," *International Journal of Hydrogen Energy*, vol. 46, no. 2, pp. 2128–2142, 2021.

[33] S. Jayabal, G. Saranya, D. Geng, L.-Y. Lin, and X. Meng, "Insight into the correlation of Pt–support interactions with electrocatalytic activity and durability in fuel cells," *Journal of Materials Chemistry A*, vol. 8, no. 19, pp. 9420–9446, 2020.

[34] I. C. Gerber and P. Serp, "A theory/experience description of support effects in carbon-supported catalysts," *Chemical Reviews*, vol. 120, no. 2, pp. 1250–1349, 2020.

[35] Y. Peng, B. Lu, N. Wang, L. Li, and S. Chen, "Impacts of interfacial charge transfer on nanoparticle electrocatalytic activity towards oxygen reduction," *Physical Chemistry Chemical Physics*, vol. 19, no. 14, pp. 9336–9348, 2017.

[36] C. Jackson, G. T. Smith, D. W. Inwood et al., "Electronic metal-support interaction enhanced oxygen reduction activity and stability of boron carbide supported platinum," *Nature Communications*, vol. 8, no. 1, article 15802, 2017.

[37] G. Chen, H. Zhong, and X. Feng, "Active site engineering of single-atom carbonaceous electrocatalysts for the oxygen reduction reaction," *Chemical Science*, vol. 12, no. 48, pp. 15802–15820, 2021.

[38] A. Austin, G. A. Petersson, M. J. Frisch, F. J. Dobek, G. Scalmani, and K. Throssell, "A density functional with spherical atom dispersion terms," *Journal of Chemical Theory and Computation*, vol. 8, no. 12, pp. 4989–5007, 2012.

[39] H. Kruse, L. Goerigk, and S. Grimme, "Why the standard B3LYP/6-31G∗ model chemistry should not be used in DFT calculations of molecular thermochemistry: understanding and correcting the problem," *The Journal of Organic Chemistry*, vol. 77, no. 23, pp. 10824–10834, 2012.

[40] T. Lu and F. Chen, "Multiwfn: a multifunctional wavefunction analyzer," *Journal of Computational Chemistry*, vol. 33, no. 5, pp. 580–592, 2012.

[41] N. Gao, B. Li, Y. Zhang et al., "CoFe alloy-decorated interlayer with a synergistic catalytic effect improves the electrochemical kinetics of polysulfide conversion," *ACS Applied Materials & Interfaces*, vol. 13, no. 48, pp. 57193–57203, 2021.

[42] N. Lawes, I. E. Gow, L. R. Smith et al., "Methanol synthesis from CO2 and H2 using supported Pd alloy catalysts," *Faraday Discussions*, vol. 242, pp. 193–211, 2023.

[43] M. A. Ahsan, A. R. Puente Santiago, M. F. Sanad et al., "Tissue paper-derived porous carbon encapsulated transition metal nanoparticles as advanced non-precious catalysts: carbon-shell influence on the electrocatalytic behaviour," *Journal of Colloid and Interface Science*, vol. 581, no. Part B, pp. 905–918, 2021.

[44] K. Kim, K. Min, Y. Go et al., "FeCo alloy nanoparticles embedded in N-doped carbon supported on highly defective ketjenblack as effective bifunctional electrocatalysts for rechargeable Zn–air batteries," *Applied Catalysis B: Environmental*, vol. 315, article 121501, 2022.

[45] S. Pradhan, K. Mishra, and Y. R. Lee, "Support-free Pd3Co NCs as an efficient heterogeneous nanocatalyst for new organic transformations of C–C coupling reactions," *Chemistry – A European Journal*, vol. 25, no. 46, pp. 10886–10894, 2019.

[46] D. Bhalothia, L. Shuan, Y.-J. Wu, C. Yan, K.-W. Wang, and T.-Y. Chen, "A highly mismatched NiO2-to-Pd hetero-structure as an efficient nanocatalyst for the hydrogen evolution reaction," *Sustainable Energy & Fuels*, vol. 4, no. 5, pp. 2541–2550, 2020.

[47] J. Jiang, Y. Fang, Y. Zhao, L. Zhao, and B. Jin, "One-step annealing synthesis of Co core-PdZn intermetallic shell composite as a bifunctional oxygen electrocatalyst for zinc-air batteries," *Molecular Catalysis*, vol. 547, article 113313, 2023.

[48] W. Zhang, X. Jiang, Z. Dong et al., "Porous Pd/NiFeOx nanosheets enhance the pH-universal overall water splitting," *Advanced Functional Materials*, vol. 31, no. 51, article 2107181, 2021.

[49] M. R. Kandel, U. N. Pan, P. P. Dhakal et al., "Unique heterointerface engineering of Ni2P–MnP nanosheets coupled Co2P nanoflowers as hierarchical dual-functional electrocatalyst for highly proficient overall water-splitting," *Applied Catalysis B: Environmental*, vol. 331, article 122680, 2023.

[50] P. P. Dhakal, U. N. Pan, M. R. Kandel et al., "Cobalt phosphide integrated manganese-doped metallic 1T-vanadium disulfide: unveiling a 2D-2D tangled 3D heterostructure for robust water splitting," *Chemical Engineering Journal*, vol. 473, article 145321, 2023.

[51] U. N. Pan, M. R. Kandel, A. K. Tomar, N. H. Kim, and J. H. Lee, "Synchronous Surface-Interface and Crystal-Phase Engineered Multifaceted Hybrid Nanostructure of Fe-(1T)-VSe2 Nanosheet and Fe-CoSe2 Nanorods Doped with P for Rapid HER and OER, Kinetics," *Small*, vol. 20, no. 7, 2024.

[52] N. Bhuvanendran, M. G. Choi, D. Kim, and S. Y. Lee, "Improved trifunctional electrocatalytic performance of integrated Co3O4 spinel oxide morphologies with abundant oxygen vacancies for oxygen reduction and water-splitting reactions," *Journal of Alloys and Compounds*, vol. 935, article 168079, 2023.

[53] N. Bhuvanendran, S. Ravichandran, K. Peng, S. S. Jayaseelan, Q. Xu, and H. Su, "Highly durable carbon supported Fe-N nanocrystals feature as efficient bi-functional oxygen electrocatalyst," *International Journal of Energy Research*, vol. 44, no. 11, pp. 8413–8426, 2020.

[54] Y. Kumar, E. Kibena-Põldsepp, J. Kozlova et al., "Bifunctional oxygen electrocatalysis on mixed metal phthalocyanine-modified carbon nanotubes prepared via pyrolysis," *ACS Applied Materials & Interfaces*, vol. 13, no. 35, pp. 41507–41516, 2021.

[55] N. Bhuvanendran, S. Ravichandran, S. Kumar, S. Y. Lee, and H. Su, "Boosting the oxygen bifunctional activity on cobalt nanocrystals/RGO with extended durability," *Materials Today Sustainability*, vol. 24, article 100596, 2023.

[56] P. Zhu, X. Xiong, X. Wang et al., "Regulating the FeN4moiety by constructing Fe–Mo dual-metal atom sites for efficient electrochemical oxygen reduction," *Nano Letters*, vol. 22, no. 23, pp. 9507–9515, 2022.